Broadly tunable and robust UV laser generation on a chip

ASGER BRIMNES GARDNER,[1,2,*] KEVIN BACH GRAVESEN,[1] JACOB CHRISTIAN LOFT,[3] PETER TØNNING,[1] ERIC J. STANTON,[4] EMIL ZANCHETTA ULSIG,[1,2] AND NICOLAS VOLET[1,2]

[1] *UVL A/S, Aarhus, Denmark*
[2] *Aarhus University, Department of Electrical and Computer Engineering, Aarhus, Denmark*
[3] *Aarhus University, Department of Physics and Astronomy, Aarhus, Denmark*
[4] *EMode Photonix, Boulder, CO, USA*
[*] *aga@ece.au.dk*

Abstract: We present a detailed characterization of a hybrid photonic platform for robust and broadly tunable ultraviolet (UV) laser generation using Čerenkov nonlinear frequency conversion (CNFC). By integrating silicon nitride waveguides with barium borate (BBO) cladding, the platform achieves UV emission across an unprecedented wavelength range of 222–319 nm. Compared to state-of-the-art UV photonic devices, our approach addresses longstanding challenges in spectral range, tunability, and integration. Theoretical modeling and experimental validation demonstrate remarkable fabrication tolerance, maintaining phase matching over a 1500 nm waveguide width variation. These findings offer a compact, scalable solution addressing critical needs in disinfection, quantum technologies, and free-space optical communication.

1. Introduction

The development of compact and efficient ultraviolet (UV) sources remains a critical challenge in photonics, despite decades of research. UV lasers are essential for advancing non-line-of-sight free-space communication [1–3], deep-UV Raman spectroscopy [4,5], precision metrology [6,7], atomic transitions for quantum applications [8,9] and human-safe disinfection [10–13]. While existing solutions, such as bulk optical systems [14–16] perform well in controlled environments, their large footprints, narrow spectral tunability and high costs hinder their scalability and practical deployment [17,18]. These limitations emphasize the need for robust, tunable, and integrated UV sources capable of addressing diverse technological demands.

Nonlinear optical techniques offer promising pathways for UV generation [19,20]. Among these, Čerenkov nonlinear frequency conversion (CNFC) is particularly attractive due to its tolerance to fabrication variations and its potential for broadband emission. Despite extensive use in the near-infrared and the visible [21–25], it has seen limited exploration in integrated photonic platforms for UV generation, largely due to material and fabrication constraints. Unlocking its potential in this spectral range could provide a transformative solution to the challenges faced by conventional solid-state and bulk optical systems.

In this work, we characterize a hybrid photonic platform that integrates silicon nitride (Si_3N_4) waveguides with barium borate (BBO) cladding, achieving robust and tunable UV laser generation over an ultra-broad wavelength range of 222–319 nm. This platform combines the scalability and low-loss properties of Si_3N_4 with the strong second-order nonlinearity and broad transparency of BBO. These unique features enable phase matching to be maintained over a 2000 nm variation in waveguide width, demonstrating exceptional fabrication tolerance. By bridging gaps in spectral range, tunability, and integration, this work establishes foundational design principles for next-generation UV photonic systems.

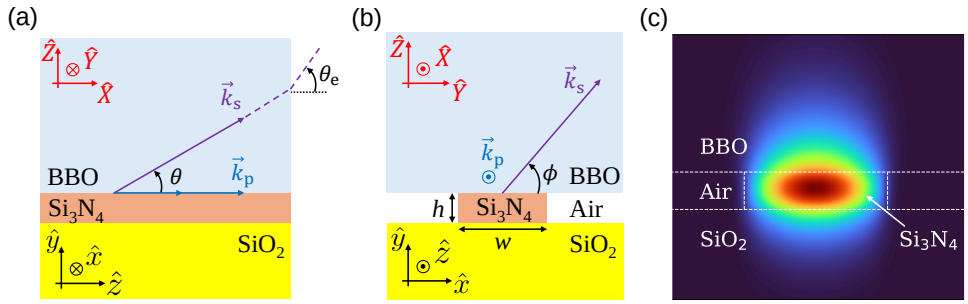

Fig. 1. Hybrid photonic platform design for Čerenkov nonlinear frequency conversion (CNFC). (a) Longitudinal cross-section of the waveguide, illustrating the silicon nitride (Si_3N_4) core with barium borate (BBO) cladding. Geometric axes (black) and BBO crystal axes (red) are shown alongside wavevectors $\vec{k}_p$ (pump) and $\vec{k}_s$ (signal), with the elevation angle θ and the refraction-adjusted emission angle θ_e labeled. (b) Cross-sectional view of the waveguide facet, detailing the waveguide thickness h and width w as well as the azimuthal angle ϕ. (c) Simulated $\mathfrak{e}_x$-field distribution for the TE-0 mode at a 445 nm pump wavelength, demonstrating optical confinement in a 100 nm thick and 1500 nm wide waveguide.

2. Design and fabrication

The hybrid photonic platform integrates Si_3N_4 waveguides with BBO cladding to leverage complementary material properties. Si_3N_4 provides scalability, low optical losses, and compatibility with standard photonic fabrication, while BBO offers strong second-order nonlinearity and broad transparency critical for efficient UV generation [26]. The device design is depicted in Fig. 1(a) and Fig. 1(b), with key parameters including the elevation angle (θ), refraction-adjusted emission angle (θ_e), and azimuthal angle (ϕ).

Efficient CNFC is achieved through evanescent overlap between the guided pump mode in the Si_3N_4 waveguide and the nonlinear BBO cladding. Simulations performed using the finite-difference method [27] confirm this overlap, as shown in Fig. 1(c). The effective refractive index of the pump mode (n_p) is obtained from these simulations and must satisfy the Čerenkov phase-matching condition [24]:

$$n_s \cos(\theta_c) = n_p, \tag{1}$$

where n_s is the refractive index of the second-harmonic signal, and θ_c is the Čerenkov elevation angle.

We deposited 100 nm stoichiometric Si_3N_4 films on oxidized silicon substrates using low-pressure chemical vapor deposition (LPCVD). Challenges included controlling thickness, minimizing sidewall roughness, and ensuring robust integration with the BBO cladding. To address these, waveguides were patterned via deep-UV lithography, ensuring accurate feature sizes, and defined using inductively coupled plasma reactive ion etching (RIE) to achieve smooth sidewalls, minimizing optical losses. Dispersion properties were characterized through ellipsometry on a test wafer to refine design parameters and ensure phase-matching conditions (details provided in Supplement 1). Chips were diced and hydrophilically bonded to 1 mm-thick BBO samples. This process required activation of bonding surfaces using oxygen plasma treatment, followed by annealing at 250 °C for six hours to increase the bond strength. To enhance coupling efficiency of pump lasers, the Si_3N_4-BBO facets were finely polished. Additionally, the top facet of the BBO was roughly polished to improve transparency and facilitate pump laser alignment.

Simulations in Figure 2 illustrate that phase matching is achieved across a broad range of waveguide widths (500–2500 nm) and pump wavelengths (400–800 nm). The dispersion model

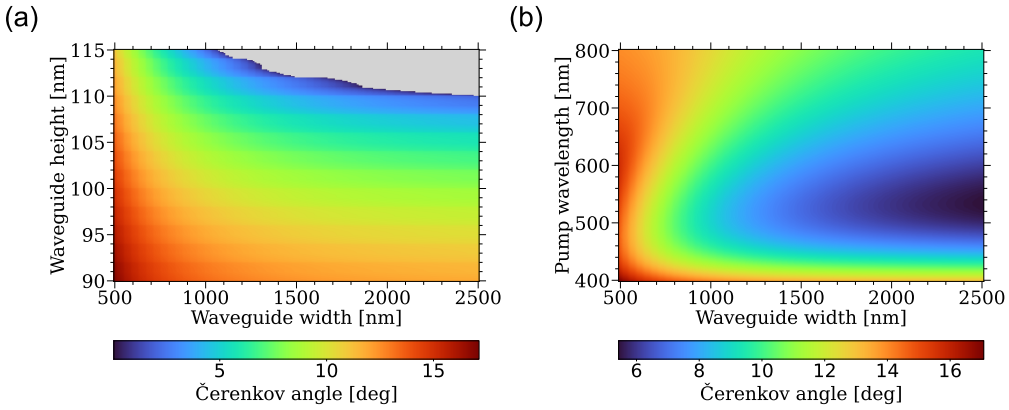

Fig. 2. Simulated Čerenkov angles for the hybrid photonic platform. (a) Dependence of Čerenkov angle on waveguide width and thickness at a fixed pump wavelength of 445 nm. Shaded regions indicate dimensions where phase matching is not achieved. (b) Variation of Čerenkov angle with waveguide width and pump wavelength for a fixed waveguide thickness of 100 nm. These simulations highlight the platform's ability to achieve phase matching across a broad range of design parameters.

used for the SiN waveguide core is sourced from [28].

The mechanism of CNFC in waveguides was analyzed using coupled-mode theory [23–25]. Building on this framework, we developed a three-dimensional vectorial model (detailed in Supplement 1) that accurately captures the non-collinear wavevector of the second-harmonic signal. This model incorporates an angle-dependent coupling coefficient κ derived from mode profiles and material nonlinearities, enabling precise characterization of the signal's angular power distribution P_s. The coupling coefficient κ quantifies the interaction strength between the guided pump mode and the radiated Čerenkov signal, considering the field overlap and polarization-dependent nonlinearities. By integrating this parameter into a fully three-dimensional treatment, the model accurately captures the interplay between elevation and azimuthal angles, enabling more accurate predictions of far-field emission profiles.

The quasi-TE guided pump mode, with its primary field amplitude along the $\hat{x}$-axis, couples to TE radiation modes of the second-harmonic signal. Analytical expressions derived from prior studies [24] were used to compute κ, as plotted in Fig. 3(a). The Čerenkov angle, determined for the cross-section in Fig. 1(c), is marked by the dashed white line in Fig. 3(a) and (b). As shown in Fig. 3(b), the simulated signal amplitude is concentrated near the Čerenkov angle, with sidelobes forming due to the characteristic sinc^2-shaped dispersion of frequency conversion. In contrast, the azimuthal angle distribution remains broad, reflecting robust phase matching across a wide angular range.

The effective index n_p of the guided pump mode is determined by the waveguide geometry, resulting in distinct Čerenkov angles for waveguides with different dimensions, as shown in Fig. 2(a). In multimode waveguides, higher-order modes contribute additional Čerenkov angles, leading to multiple emission lobes, a phenomenon previously observed in lithium niobate waveguides [29].

In this study, Čerenkov secondh-harmonic generation emission was simulated for pump wavelengths of 445 nm (blue), 517 nm (green), and 640 nm (red). The far-field signal distributions are plotted in Fig. 4 for a 1500 nm wide, 100 nm thick waveguide, and a pump propagation length of 1 mm. The plotted distributions account for refraction at the BBO-air interface. Since the selected waveguide dimensions support multimode propagation, contributions from the first three guided modes are presented for each pump wavelength, except for the TE-2 mode at 640

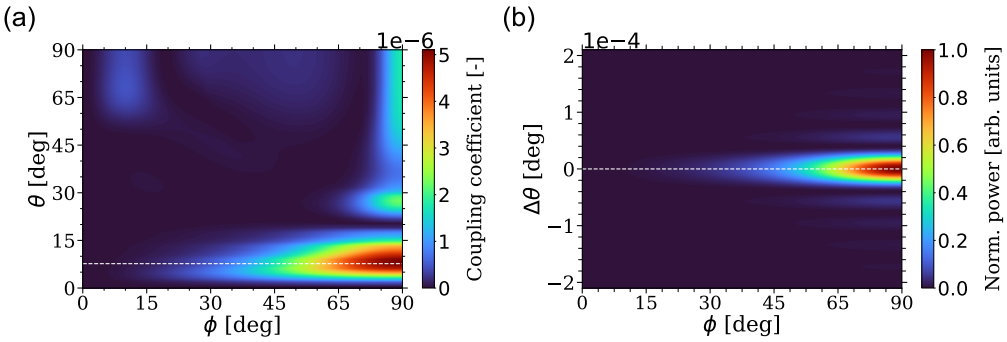

Fig. 3. Simulated coupling and angular power distribution for Čerenkov emission. (a) Coupling coefficient κ derived from the simulated mode profile in Fig. 1(c), plotted as a function of elevation angle θ and azimuthal angle ϕ. (b) Normalized angular power distribution of the Čerenkov signal after 1 mm of pump propagation. Dashed white lines indicate the calculated Čerenkov angle θ_C, while the angular deviation $\Delta\theta = \theta - \theta_C$ reveals sinc^2-shaped dispersion effects characteristic of frequency conversion.

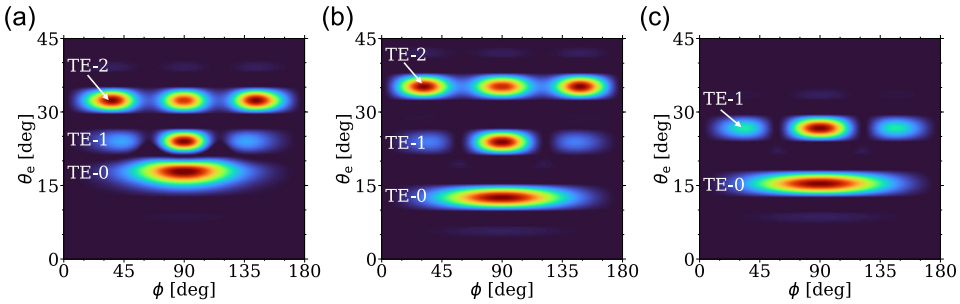

Fig. 4. Simulated far-field distributions of the Čerenkov second-harmonic signals. Emission patterns are shown for wavelengths of (a) 222 nm, (b) 258 nm, and (c) 320 nm for a 100 nm thick and 1500 nm wide waveguide. Each angular lobe corresponds to harmonics generated by different pump modes, highlighting the impact of waveguide geometry and multimode propagation on far-field emission profiles.

nm, which is not supported. Each pump mode generates a distinct Čerenkov signal at a specific emission angle, with mode-dependent variations in the azimuthal angle distribution.

3. Experimental characterization

To characterize the far-field distribution of the generated UV signals, we designed a custom chip-stage goniometer capable of capturing spatial and spectral variations. These include broad azimuthal distributions, elevation angle dependencies, and multiple emission lobes arising from multimode waveguides with varying dimensions and pump wavelengths. The setup, as illustrated in Fig. 5, employs two independent rotational stages to scan polar and azimuthal angles within a spherical coordinate system centered on the chip's output facet.

A solarization-resistant multimode fiber (core diameter: 600 µm, acceptance angle: 12.7°), connected to a spectrometer, is mounted on an adjustable arm. The spectrometer—either an Ocean Optics Maya2000Pro (165–275 nm) or a StellarNet BlackComet (200–600 nm)— enables complete spatial and spectral mapping of the far-field UV emission.

The UV signals were generated by pumping the waveguide with diode lasers at various wavelengths. For blue light, a stabilized external-cavity diode laser (ECDL, Toptica DL pro)

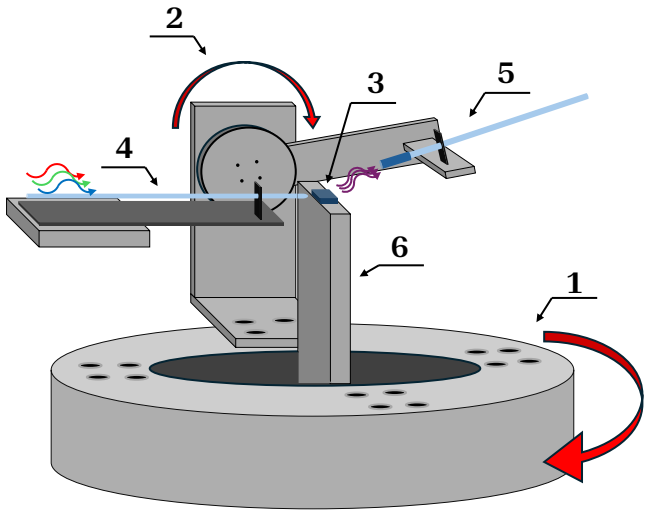

Fig. 5. Goniometric setup for far-field measurements. The setup includes: (1) primary rotation stage, (2) secondary rotation stage, (3) conversion chip, (4) input fiber for the pump laser, (5) output fiber connected to a spectrometer, and (6) centered chip stage. This configuration enables precise angular mapping of the far-field emission.

at 445 nm and a stabilized diode laser (Hübner Photonics Cobolt08) at 473 nm were used. For green and red, single-mode diode lasers (Toptica iBeam smart) operating at 517 nm and 640 nm, respectively, were employed. A polarization-maintaining (PM) lensed fiber was used to edge-couple the pump lasers to the chip, ensuring stable coupling. The detector fiber was positioned 8 cm from the chip's output facet for all measurements.

3.1. Broadband frequency conversion to the UV

Figure 6 shows the measured UV emission spectra spanning an ultra-broadband range of 222–319 nm, consistent with the phase-matching predictions in Fig. 2. Phase-matching is achieved through second-harmonic generation (SHG, solid lines) and sum-frequency generation (SFG, dashed lines). These spectra were obtained from a single 1500 nm wide waveguide, highlighting the exceptional conversion bandwidth enabled by the Čerenkov approach. As in previous studies [26], the signal were measured after reflection at the top BBO surface, dictated by the chip geometry.

The observed peak broadening above 260 nm is attributed to the lower spectral resolution of the BlackComet compared to the Maya2000Pro and the lower frequency noise of the 445 nm pump laser. The minor offsets between pump and signal wavelengths are consistent with drift in the pump laser wavelength.

3.2. Far-field distributions

Figure 7 presents the measured two-dimensional angular distributions of the signal at an emission wavelength of 258 nm for waveguide widths ranging from 750 nm to 2500 nm. The intensity at each point was obtained by integrating the counts within the measured spectrometer peak. As predicted by the simulations in Fig. 4, the signal forms a dominant fundamental lobe, with additional higher-order lobes emerging in wider waveguides due to multimode propagation. The emission is concentrated within narrow elevation angle bands near the Čerenkov angles, while

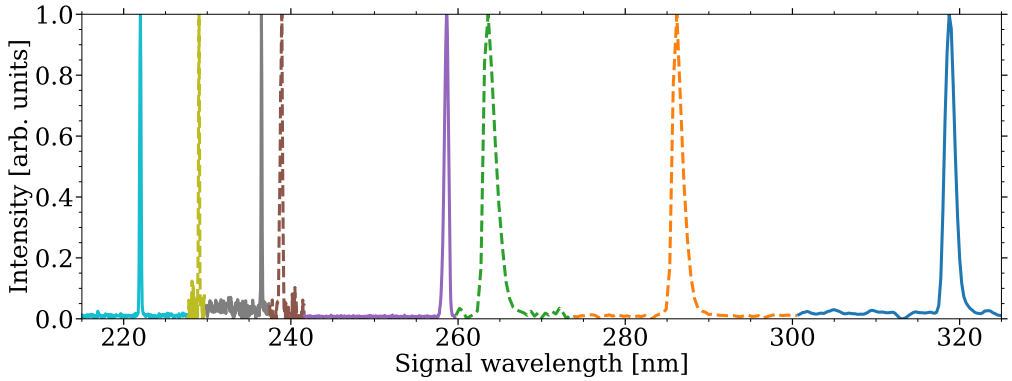

Fig. 6. Measured UV emission spectra demonstrating broadband phase matching in the hybrid photonic platform. The spectra span 222–319 nm, with emission recorded at specific wavelengths of 222 nm, 229 nm, 236 nm, 239 nm, 258 nm, 262 nm, 286 nm and 319 nm. The spectra were obtained from a single 1500 nm wide waveguide using various pump lasers. Solid lines represent second-harmonic generation (SHG), while dashed lines correspond to sum-frequency generation (SFG).

the azimuthal angle remains broad. A slight broadening of the elevation angle distribution, proportional to the pump's propagation length, is observed. Conversely, a narrowing trend in the azimuthal distribution is evident for wider waveguides. Figure 8 further explores this trend by comparing measured and simulated far-field distributions for waveguides widths of 750 nm and 2000 nm. The simulated and measured distributions demonstrate strong agreement, confirming the narrowing of the azimuthal emission profile as the waveguide width increases. This narrowing reflects the reduced angular spread of the signal in multimode configurations, highlighting the critical role of waveguide geometry in shaping emission patterns.

Figures 7 and 8 consistently show a fundamental emission lobe for all waveguide widths. In Fig. 7(a), this fundamental lobe dominates the emission profile, while traces of higher-order lobes emerge in the wider waveguides, as seen in Fig. 7(b) and (c). For the 2500 nm wide waveguide shown in Fig. 7(d), the signal intensity shifts primarily into the first higher-order lobe. These variations in emission patterns align with the degrees of higher-order mode propagation predicted in Fig. 4. To confirm this behavior, Fig. 9 demonstrates selective coupling into the TE-0, TE-1, and TE-2 pump modes for an emission wavelength of 222 nm. Adjusting the position of the input fiber modifies the modal overlaps between the fiber mode and the waveguide modes, resulting in distinct angular signal distributions. These distributions reveal shifts in the primary emission lobe to larger angles and increasingly complex patterns, consistent with theoretical predictions in Fig. 4.

To further validate the theoretical model, and to demonstrate the robustness of the CNFC approach, Fig. 10 compares the measured elevation angles of the lowest-order signal lobes to the simulated elevation angles for the TE-0 pump modes across three pump wavelengths and various waveguide widths. The simulated elevation angles were derived from the Čerenkov angle, as defined by Eq. (1) and accounting for refraction at the BBO-air facet, using the dispersion model obtained from the reference wafer through ellipsometry. The results show a clear correlation between waveguide width and emission angle, closely matching the predicted trends for all pump wavelengths. Notably, for the 750 nm wide waveguide, emission was observed only with the 517 nm pump.

The azimuthal angle distribution in Fig. 7(d) and Fig. 9 appears slightly skewed compared to the elevation angle distribution, likely due to a minor misalignment of the chip on the goniometer stage.

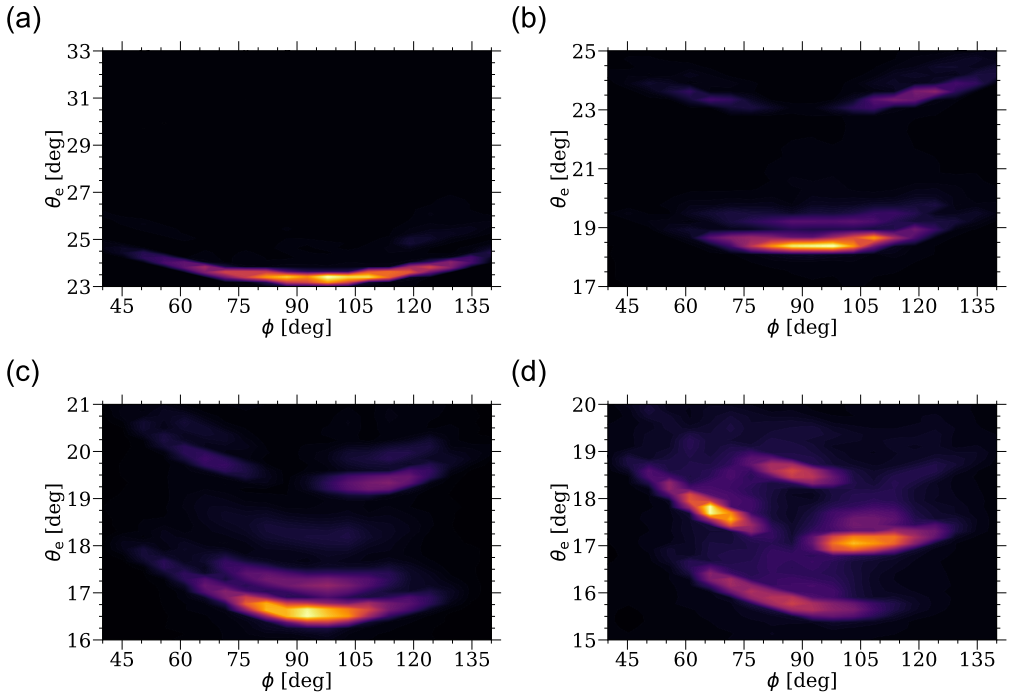

Fig. 7. Far-field distributions of the 258 nm emission for varying waveguide widths. Measured distributions are shown for waveguide widths of (a) 750 nm, (b) 1250 nm, (c) 1750 nm, and (d) 2500 nm. The profiles illustrate how waveguide width affects emission characteristics, with narrower waveguides producing simpler angular patterns and wider waveguides exhibiting higher-order lobes due to multimode propagation.

A small angular deviation relative to the detector arm can introduce asymmetry in the measured signal. Additionally, slight curvature in the lobes at extreme azimuthal angles, as seen in Fig. 7, is attributed to partial reflections at the BBO-air interface. These two-dimensional measurements require several minutes to complete, during which mechanical drift in the input coupling can occur. To mitigate this, the system was allowed to stabilize for 30 minutes before each sweep, with drift actively monitored throughout. Nevertheless, variations in coupling efficiency between waveguides were observed, likely stemming from inconsistencies in facet polishing. Future fabrication processes could address these challenges by adopting chemical etching techniques to produce smoother and more consistent facets [30]. Furthermore, propagation losses, which are influenced by interfacial scattering and material absorption, become more pronounced in narrower waveguides due to tighter mode confinement [31]. To achieve optimal conversion efficiency, waveguide designs should balance small modal areas for enhanced nonlinear interaction with reduced interfacial scattering. This trade-off is critical for maximizing performance in integrated UV photonic devices.

4. Discussion and conclusion

Our simulations and measurements establish a robust foundation for optimizing Čerenkov nonlinear frequency conversion (CNFC)-based UV devices. This work demonstrates a hybrid photonic platform that achieves ultra-broadband UV generation across a 195 nm pump wavelength span, with phase-matching maintained for waveguide widths spanning over 1500 nm. As shown in Fig. 6 and Fig. 10, these results highlight the platform's exceptional fabrication tolerance and

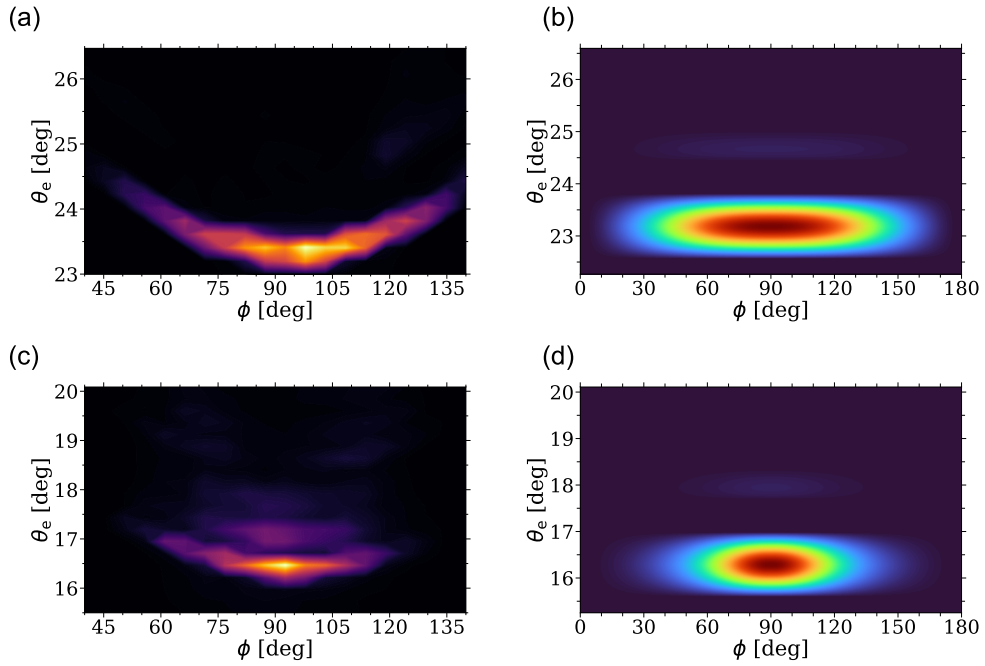

Fig. 8. Comparison of measured and simulated far-field distributions for the TE-0 mode at 258 nm. Distributions are shown for waveguide widths of 750 nm: (a) measured and (b) simulated, and 2000 nm: (c) measured and (d) simulated. The results demonstrate the narrowing of the azimuthal emission profile with increasing waveguide width, with strong agreement between measurements and simulations.

scalability, enabling robust and tunable UV emission across a wide spectral range. These features represent a significant advancement in integrated photonics, offering compact and versatile UV sources tailored for diverse applications.

Mapping two-dimensional emission profiles (Fig. 7) reveals key trade-offs in waveguide design. Narrower waveguides enhance beam quality by concentrating output power into a single emission lobe, but broader azimuthal distributions may complicate directional applications. In contrast, wider waveguides provide narrower beam profiles, but introduce multimode propagation and hence stricter input coupling tolerances, as illustrated in Fig. 9. Addressing these trade-offs through tailored geometries or mode filters could further enhance the platform's adaptability for specific use cases.

Our results align with prior demonstrations, such as those in [32], where CNFC was achieved by focusing a Gaussian beam onto a domain wall with varying second-order nonlinearity. However, the work presented here extends the concept significantly by offering a scalable platform with broad spectral coverage and exceptional fabrication tolerances. These features, combined with the inherent advantages of integrated photonics, position this platform as a transformative solution for next-generation UV devices.

The demonstrated ability to generate UV light across a wide spectral range directly addresses critical challenges in quantum technologies, disinfection, and optical communication. The platform's compact and scalable far-UVC light generation at 222 nm (as shown in Fig. 2) aligns with the growing demand for safe and efficient pathogen inactivation solutions in healthcare and public spaces. The spectral tunability makes the platform highly relevant for applications requiring precise UV emission, such as atomic transitions used in quantum sensing and

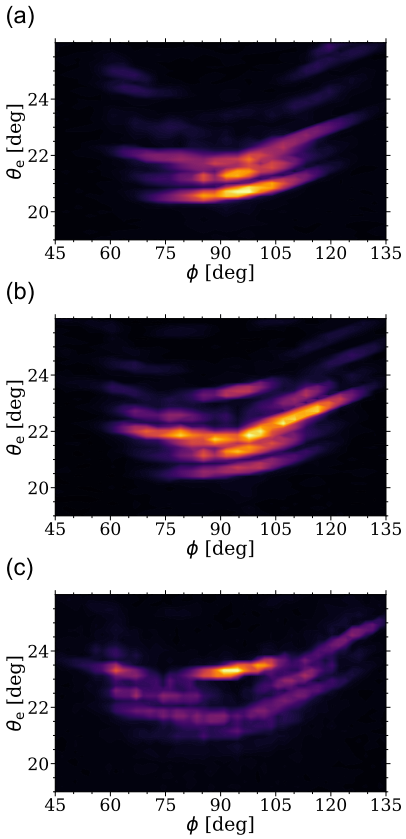

Fig. 9. Far-field measurements of the 222 nm emission from a 2000 nm wide waveguide. Input coupling is optimized to selectively excite (a) TE-0, (b) TE-1, and (c) TE-2 modes. Selective coupling shifts the primary emission lobe to different angles, as predicted in Fig. 4, demonstrating the mode-dependent angular distribution of the second-harmonic signal.

metrology. Additionally, the platform supports advancements in free-space optical communication, particularly in non-line-of-sight (NLOS) scenarios, where the shorter wavelengths of UV light scatter more effectively in the atmosphere. This scattering capability enables communication around obstacles or through particulate-heavy environments, making the platform well-suited for specialized free-space communication challenges.

While our simulations successfully predict the general trends of azimuthal broadening and lobe formation for higher-order pump modes, minor deviations from measured emission profiles suggest the influence factors such as surface roughness, coupling instabilities, or fabrication variations. Incorporating these effects into future models will improve predictive accuracy and further optimize device performance.

This hybrid photonic platform offers a promising foundation for advancing integrated UV photonics. Future research could explore alternative geometries and nonlinear materials to extend the wavelength range or improve conversion efficiency. Further developments in beam shaping and emission control would broaden the platform's applications, solidifying its role as a foundational technology for quantum systems, secure optical communication, and scalable disinfection solutions.

Funding. Innovationsfonden (3129-00077B)

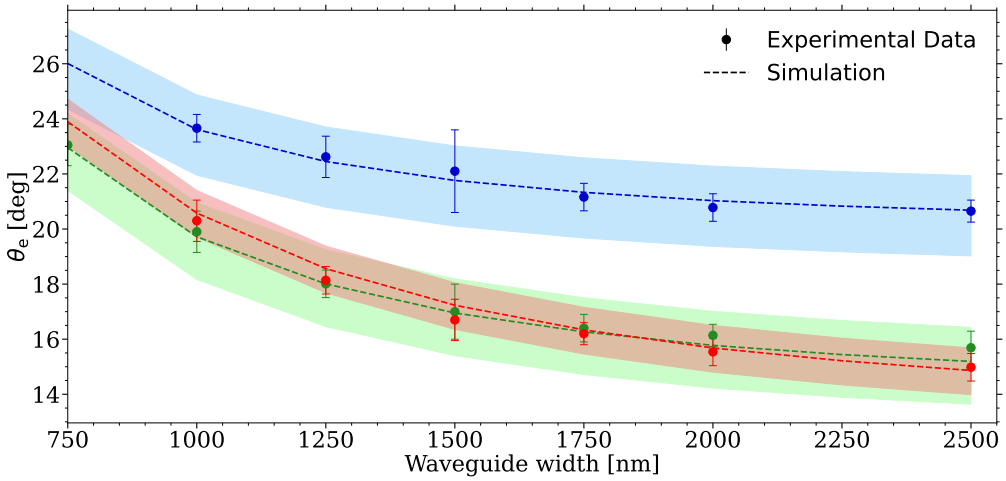

Fig. 10. Simulated and measured Čerenkov angles as a function of waveguide width for the TE-0 mode. Results are shown for signal wavelengths of 222 nm (blue), 258 nm (green), and 320 nm (red). Simulations assume a 100 nm thick waveguide, with shaded areas indicating a ±3 nm uncertainty in thickness. Experimental results closely match simulated trends, confirming the dependence of emission angles on waveguide width. For the 750 nm wide waveguide, coupling was achieved only for the 258 nm signal.

Acknowledgments. We gratefully acknowledge Toptica for providing the iBeam Smart lasers used in this study.

Disclosures. ABG: UVL A/S (F, E), KBG: UVL A/S (E), PT: UVL A/S (E), EJS: EMode Photonix (I, E), UVL A/S (C), EZU: UVL A/S (I, E), NV: UVL A/S (I, E)

Disclosures. The authors declare no conflicts of interest.

Data Availability Statement. Data underlying the results presented in this paper will be made publicly available on Zenodo upon publication.

Supplemental document. See Supplement 1 for supporting content.

References

1. D. M. Maclure, C. Chen, J. J. D. McKendry, *et al.*, "Hundred-meter Gb/s deep ultraviolet wireless communications using AlGaN micro-LEDs," Opt. Express **30**, 46811–46821 (2022).
2. T. Shan, R. Yuan, N. He, and J. Cheng, "Non-line-of-sight ultraviolet transmission coverage in non-precipitating, foggy, and rainy weather," Opt. Express **31**, 37703–37721 (2023).
3. Z. Qi, L. Wang, Y. Liang, *et al.*, "Deep-ultraviolet light communication in sunlight using 275-nm LEDs," Appl. Phys. Lett. **123**, 161109 (2023).
4. M. Foster, W. Brooks, P. Jahn, *et al.*, "Demonstration of a compact deep UV Raman spatial heterodyne spectrometer for biologics analysis," J. Biophotonics **15**, e202200021 (2022).
5. D. P. Gulo, N. T. Hung, W.-L. Chen, *et al.*, "Interacting phonons between layers in Raman spectra of carbon nanotubes inside boron nitride nanotubes," The J. Phys. Chem. Lett. **14**, 10263–10270 (2023).
6. M. E. Kim, W. F. McGrew, N. V. Nardelli, *et al.*, "Improved interspecies optical clock comparisons through differential spectroscopy," Nat. Phys. **19**, 25–29 (2023).
7. C. Zhang, T. Ooi, J. Higgins, *et al.*, "Frequency ratio of the ^{229m}Th nuclear isomeric transition and the ^{87}Sr atomic clock," Nature **633**, 63–70 (2024).
8. T. R. Tan, J. P. Gaebler, Y. Lin, *et al.*, "Multi-element logic gates for trapped-ion qubits," Nature **528**, 380–383 (2015).
9. S. C. Burd, J.-P. Penttinen, P.-Y. Hou, *et al.*, "VECSEL systems for quantum information processing with trapped beryllium ions," J. Opt. Soc. Am. B **40**, 773 (2023).
10. M. Buonanno, D. Welch, I. Shuryak, and D. J. Brenner, "Far-UVC light (222 nm) efficiently and safely inactivates airborne human coronaviruses," Sci. Reports **10**, 10285 (2020).
11. D. Welch, N. J. Kleiman, P. C. Arden, *et al.*, "No evidence of induced skin cancer or other skin abnormalities after long-term (66 week) chronic exposure to 222-nm far-UVC radiation," Photochem. Photobiol. **99**, 168–175 (2023).

12. Q. Luo, J. Ma, M. Wang, *et al.*, "All-solid-state far-UVC pulse laser at 222 nm wavelength for UVC disinfection," Chin. Opt. Lett. **21**, 011401 (2023).
13. J. Schleusener, S. B. Lohan, L. Busch, *et al.*, "Irradiation of human oral mucosa by 233 nm far UV-C LEDs for the safe inactivation of nosocomial pathogens," Sci. Reports **13**, 22391 (2023).
14. B. Willenberg, F. Brunner, C. R. Phillips, and U. Keller, "High-power picosecond deep-UV source via group velocity matched frequency conversion," Optica **7**, 485–491 (2020).
15. K. L. Corre, A. Barnini, T. Robin, *et al.*, "Watt-level deep-UV subnanosecond laser system based on Nd-doped fiber at 229 nm," Opt. Lett. **48**, 1276–1279 (2023).
16. Z. Cui, J. Xu, C. Lu, *et al.*, "High-power picosecond UV and deep-UV laser sources delivering powers of 30 W at 355 nm, 10 W at 266 nm, and 5 W at 213 nm," Opt. Lett. **49**, 6497–6500 (2024).
17. M. Kneissl, T.-Y. Seong, J. Han, and H. Amano, "The emergence and prospects of deep-ultraviolet light-emitting diode technologies," Nat. Photonics **13**, 233–244 (2019).
18. H. Amano, R. Collazo, C. D. Santi, *et al.*, "The 2020 UV emitter roadmap," J. Phys. D: Appl. Phys. **53**, 503001 (2020).
19. N. Ruhnke, A. Muller, B. Eppich, *et al.*, "Compact deep UV system at 222.5 nm based on frequency doubling of GaN laser diode emission," IEEE Photonics Technol. Lett. **30**, 289–292 (2018).
20. T. Nambu, T. Yano, S. Umeda, *et al.*, "DUV coherent light emission from ultracompact microcavity wavelength conversion device," Opt. Express **30**, 18628–18637 (2022).
21. J. Ohya, G. Tohmon, K. Yamamoto, *et al.*, "Picosecond blue light pulse generation by frequency doubling of a gain-switched GaAlAs laser diode with saturable absorbers," Appl. physics letters **56**, 2270–2272 (1990).
22. K. Yamamoto, H. Yamamoto, and T. Taniuchi, "Simultaneous sum-frequency and second-harmonic generation from a proton-exchanged MgO-doped LiNbO3 waveguide," Appl. Phys. Lett. **58**, 1227–1229 (1991).
23. H. Tamada, "Coupled-mode analysis of second harmonic generation in the form of Cerenkov radiation from a planar optical waveguide," IEEE J. Quant. Electron. **27**, 502–508 (1991).
24. T. Suhara, T. Morimoto, and H. Nishihara, "General coupled-mode analysis of Cerenkov-radiation-type second-harmonic generation in channel and fiber waveguides," IEEE J. Quant. Electron. **29**, 525–537 (1993).
25. H. Z. Hu, X. G. Yi, and R. L. Ding, "Theoretical analysis of second harmonic generation in the form of Cherenkov radiation from a rectangular optical waveguide," Opt. Commun. **149**, 101–107 (1998).
26. E. J. Stanton, P. Tønning, E. Z. Ulsig, *et al.*, "Continuous-wave second-harmonic generation in the far-UVC pumped by a blue laser diode," Sci. Reports **14**, 3238 (2024).
27. EMode (version 0.1.1) [Software] from EMode Photonix. Available at https://emodephotonix.com/.
28. S. Martinussen, E. Berenschot, D. Bonneville, *et al.*, "Thick waveguides of low-stress stoichiometric silicon nitride on sapphire (SiNOS)," Opt. Express **32**, 36835–36847 (2024).
29. N. A. Sanford and W. C. Robinson, "Direct measurement of effective indices of guided modes in $LiNbO_3$ waveguides using the Cerenkov second harmonic," Opt. Lett. **12**, 445–447 (1987).
30. X. Ji, S. Roberts, M. Corato-Zanarella, and M. Lipson, "Methods to achieve ultra-high quality factor silicon nitride resonators," APL Photonics **6**, 071101 (2021).
31. R. Wolf, I. Breunig, H. Zappe, and K. Buse, "Scattering-loss reduction of ridge waveguides by sidewall polishing," Opt. Express **26**, 19815–19820 (2018).
32. X. Deng and X. Chen, "Domain wall characterization in ferroelectrics by using localized nonlinearities," Opt. Express **18**, 15597–15602 (2010).